

Reconstruction of Reionization Histories from 21 cm Power-Spectrum Evolution with Artificial Neural Networks

Yu-Le Wang^{1,*}, Hayato Shimabukuro¹

South-Western Institute for Astronomy Research, Key Laboratory of Survey Science of Yunnan Province,
Yunnan University, Kunming, Yunnan 650500, People's Republic of China

Received 20XX Month Day; accepted 20XX Month Day

Abstract We investigate whether the redshift evolution of the fixed- k dimensionless 21 cm power spectrum, $\Delta_{21}^2(k, z)$, contains sufficient information to reconstruct reionization histories $x_{\text{HI}}(z)$ with artificial neural networks. Using semi-numerical realizations generated within a restricted three-parameter 21cmFAST model family, we train a compact feed-forward network to learn the inverse mapping from power-spectrum trajectories to the neutral-fraction history over $6 \leq z \leq 15$. For $k = 0.1, 0.5, \text{ and } 1.0 h \text{ Mpc}^{-1}$, representative tests on an independent test set show that the midpoint redshift z_{50} is recovered more accurately than the duration $\Delta z = z_{75} - z_{25}$: z_{50} is reconstructed with MAE = 0.0046 and RMSE = 0.0100, whereas Δz yields MAE = 0.0302 and RMSE = 0.0378. This result indicates that fixed- k power-spectrum evolution carries stronger information about the timing of reionization than about the detailed width of the transition within the adopted prior. We further test an idealized foreground-free SKA1-Low-like thermal-plus-sample-variance noise model and find that the reconstruction remains stable in the favorable signal-to-noise regime considered here. These results demonstrate that neural networks can serve as prior-dependent inverse mapping for reconstructing reionization histories from 21 cm power-spectrum evolution.

Key words: dark ages — reionization — first stars — methods: data analysis — cosmology: theory

1 INTRODUCTION

The Cosmic Dawn and the Epoch of Reionization mark the interval during which the first luminous sources transformed the intergalactic medium from a predominantly neutral state into an ionized one. A central goal of early-Universe astrophysics is therefore to reconstruct the redshift evolution of the volume-averaged neutral hydrogen fraction, $x_{\text{HI}}(z)$. That history encodes when the first galaxies became efficient ionizing sources, how rapidly ionized regions grew and merged, and how radiative feedback shaped subsequent

* E-mail: wangyule@stu.ynu.edu.cn

structure formation. By $z \approx 6$, reionization was largely complete, but the timing and duration of the transition remain key open questions (e.g. Barkana & Loeb 2001; Robertson 2022).

Recent observations have made this question increasingly concrete. On the galaxy side, JWST spectroscopy is beginning to probe the luminosities, ionizing spectra, and local environments of sources well into the reionization era, while Ly α -based measurements—including absorption-line constraints from Gunn–Peterson troughs and damping wings, as well as luminosity-function and clustering studies of Ly α emitters—provide increasingly informative, though model-dependent, constraints on the neutral IGM at $z \gtrsim 6$. Joint interpretations of these data have reinforced the view that the main phase of reionization may occur relatively late, with a substantial decline in x_{HI} between $z \sim 8$ and $z \sim 6$, and in some analyses even a comparatively sharp transition, although the inferred history is not unique (Fan et al. 2006; Dayal & Ferrara 2018; Madau 2017; Umeda et al. 2025; Umeda et al. 2025; Kageura et al. 2025).

At the same time, these observables do not directly provide the full function $x_{\text{HI}}(z)$. JWST primarily constrains the abundance, spectra, and ionizing efficiency of source populations, so converting those data into a global ionization history requires assumptions about escape fractions, source demographics, and the coupling between galaxies and the surrounding IGM (Dayal & Ferrara 2018; Madau 2017). Ly α -based probes are especially informative during the late stages of reionization, but their interpretation depends on absorption-line radiative transfer and on the environments of the background sources: Gunn–Peterson and damping-wing measurements are sensitive to neutral hydrogen along particular sightlines, whereas Ly α emitter statistics respond to both IGM transmission and galaxy evolution. In addition, the Ly α forest saturates rapidly as the neutral fraction rises, which limits the direct leverage of absorption measurements on the full reionization history and increases the importance of astrophysical systematics associated with circumgalactic gas and large-scale ionized topology (Fan et al. 2006; Umeda et al. 2025; Umeda et al. 2025; Kageura et al. 2025). The motivation for additional probes is therefore not that current measurements are inadequate, but that reconstructing $x_{\text{HI}}(z)$ benefits from observables that are complementary to them and that trace neutral hydrogen in the IGM more directly.

In this context, the redshifted 21 cm signal is especially attractive. Because the differential brightness temperature depends on the density field, the neutral fraction, and the spin temperature relative to the cosmic microwave background, the 21 cm signal can in principle follow the evolution of the neutral IGM over a broad redshift range and remain sensitive to the growth, overlap, and patchiness of ionized regions (e.g., Scott & Rees 1990; Madau et al. 1997; Furlanetto et al. 2004, 2006; Pritchard & Loeb 2012; Shimabukuro et al. 2023). For interferometric experiments such as LOFAR, HERA, and SKA, the power spectrum has become the natural and most practical summary statistic, because it captures this evolving morphology in a form that can be measured before high-fidelity imaging becomes routine (Furlanetto & Briggs 2004; Zaldarriaga et al. 2004; Morales & Wyithe 2010; Koopmans et al. 2015; DeBoer et al. 2017).

Even in the 21 cm case, however, the scientific target of this paper, $x_{\text{HI}}(z)$, is not measured directly. The statistic used here is the redshift evolution of the fixed- k dimensionless power spectrum, $\Delta_{21}^2(k, z)$, so the task is to infer a reionization-history trajectory from an observable power-spectrum trajectory. Within the adopted three-parameter 21cmFAST prior, this is a nonlinear inverse map rather than a direct measurement, and it is not obvious that the relation can be reduced to a simple analytic fitting formula. Forward-modeling

frameworks based on 21cmFAST and related Bayesian inference pipelines provide an established way to constrain astrophysical parameters and average neutral fractions within explicit priors, but they are not the most direct tool for the proof-of-concept question posed here: whether this trajectory-to-trajectory inverse relation is sufficiently regular and informative to be learned within a restricted model family (Mesinger et al. 2011; Murray et al. 2020; Greig & Mesinger 2015).

This motivates the use of a compact ANN as a flexible inverse mapping. Its role in the present study is not to provide a model-independent estimator, but to test whether fixed- k trajectories of $\Delta_{21}^2(k, z)$ retain enough information to reconstruct $x_{\text{HI}}(z)$ within a restricted three-parameter 21cmFAST prior. Machine-learning methods have already been explored in several 21 cm contexts, including early ANN analyses of the 21 cm signal, CNN-based inference of reionization history from 21 cm images, ANN recovery of the H II bubble size distribution from the power spectrum, and nonlinear reconstruction of the 21 cm global signal from power-spectrum information (e.g. Shimabukuro & Semelin 2017; La Plante & Ntampaka 2019; Shimabukuro et al. 2022; Sikder et al. 2024; Shimabukuro 2025). In that spirit, we use the ANN here as a prior-dependent proof-of-concept tool and evaluate how well it reconstructs $x_{\text{HI}}(z)$ over $z = 6\text{--}15$ from simulated trajectories spanning $z = 6\text{--}30$, both in the noiseless case and under an idealized foreground-free SKA1-Low-like thermal-plus-sample-variance noise model. The remainder of this paper introduces the 21 cm observables and target histories, describes the ANN framework, and then presents representative results for both noiseless and noisy cases.

2 21CM SIGNAL, POWER SPECTRUM, AND TARGET REIONIZATION HISTORY

This section summarizes the physical quantities used throughout this work and clarifies the inverse problem addressed in the following sections. We first review the basic physics of the cosmological 21 cm signal, then define the reionization history $x_{\text{HI}}(z)$ as the target quantity to be reconstructed, and finally introduce the power spectrum as the interferometric observable used to infer it.

2.1 21 cm brightness temperature

The redshifted 21 cm hyperfine transition of neutral hydrogen is one of the most promising probes of the intergalactic medium during cosmic dawn and the epoch of reionization (Scott & Rees 1990; Madau et al. 1997; Furlanetto et al. 2006; Pritchard & Loeb 2012). Its observability depends on the spin temperature T_S , which is regulated by radiative coupling to the CMB, collisional processes, and Ly α pumping through the Wouthuysen–Field mechanism (Wouthuysen 1952; Field 1958, 1959; Hirata 2006; Chen & Miralda-Escudé 2004, 2008). In the fiducial simulations used in this work, spin-temperature fluctuations are explicitly included. The associated X-ray heating parameters are fixed to the default 21cmFAST values and are not varied within the training prior. This is a deliberate simplification: for the present proof-of-concept we vary only the parameters that most directly control the timing and morphology of reionization, so that the network learns a restricted inverse map to $x_{\text{HI}}(z)$ rather than a broader joint heating-ionization problem. Accordingly, the factor $1 - T_\gamma/T_S$ is computed self-consistently in the forward model rather than being assumed to be unity over the redshift range used for the reconstruction.

For a gas element at redshift z and comoving position \boldsymbol{x} , the differential 21 cm brightness temperature relative to the CMB can be approximated as (Mesinger 2019)

$$\delta T_b(z, \boldsymbol{x}) \cong 27(1 + \delta) x_{\text{HI}}(z, \boldsymbol{x}) \left(\frac{\Omega_{b,0} h^2}{0.023} \right) \left(\frac{0.15}{\Omega_{m,0} h^2} \frac{1+z}{10} \right)^{1/2} \left(1 - \frac{T_\gamma}{T_S} \right) \text{ mK}, \quad (1)$$

where δ is the baryon overdensity, $x_{\text{HI}}(z, \boldsymbol{x})$ is the local neutral hydrogen fraction, T_γ is the CMB temperature, and T_S is the hydrogen spin temperature. The corresponding local ionized fraction is $1 - x_{\text{HI}}(z, \boldsymbol{x})$. For simplicity, we use the approximate form above and do not explicitly include the peculiar-velocity gradient term, since the purpose of this paper is not precision forward modeling of the full 21 cm signal but the inverse reconstruction of the global reionization history.

Equation (1) makes clear that the 21 cm signal is intrinsically multivariate: it depends on the density, ionization, and thermal states of the gas, as well as on the radiation background. The mapping from a 21 cm statistic back to the global reionization history is therefore nonlinear and prior dependent. Throughout this work we assume a flat Λ CDM cosmology consistent with *Planck* 2018, with $\Omega_m = 0.315$, $\Omega_b = 0.049$, $h = 0.674$, $\sigma_8 = 0.811$, and $n_s = 0.965$ (Planck Collaboration et al. 2020).

2.2 Target reionization history

The quantity reconstructed in this paper is the volume-averaged neutral fraction $x_{\text{HI}}(z)$, which we refer to as the reionization history. When convenient, we also use the ionized volume filling factor

$$Q(z) = 1 - x_{\text{HI}}(z). \quad (2)$$

This is the natural target quantity for the present study, because it provides a compact description of the global progress of reionization and allows summary quantities such as the midpoint and duration to be defined straightforwardly.

A useful approximate description of the global reionization history is given by the photon-counting equation (Madau 2017)

$$\frac{dQ}{dt} = \frac{\langle \dot{n}_{\text{ion}} \rangle}{\langle n_{\text{H}} \rangle} - \frac{Q}{\bar{t}_{\text{rec}}}, \quad (3)$$

where $\langle \dot{n}_{\text{ion}} \rangle$ is the emission rate of ionizing photons escaping into the IGM per unit proper volume, $\langle n_{\text{H}} \rangle = 1.89 \times 10^{-7} (1+z)^3 \text{ cm}^{-3}$ is the cosmological mean hydrogen number density, and \bar{t}_{rec} is an effective recombination timescale (Madau et al. 1999). Equation (3) makes clear that reionization histories depend on both source efficiency and recombinations, so any inversion from 21 cm statistics necessarily remains sensitive to the adopted astrophysical prior.

Since the midpoint and duration of reionization play an important role in the analysis below, we define them explicitly here. Here, the ‘‘midpoint’’ simply means the epoch at which reionization is halfway complete, so that the IGM is 50% neutral on average. The midpoint redshift z_{50} is defined by

$$x_{\text{HI}}(z_{50}) = 0.5, \quad (4)$$

and the reionization duration is defined as

$$\Delta z \equiv z_{75} - z_{25}, \quad (5)$$

where $x_{\text{HI}}(z_{75}) = 0.75$ and $x_{\text{HI}}(z_{25}) = 0.25$. We adopt these thresholds because they bracket the central 50% of the transition, providing a simple measure of its width while avoiding excessive sensitivity to the slowly varying early and late tails of the history near $x_{\text{HI}} \approx 1$ and $x_{\text{HI}} \approx 0$. With this convention, Δz is always positive and quantifies the redshift width of the main reionization transition.

Recent JWST-based analyses suggest that reionization may have been relatively late and rapid, with a steep decline in x_{HI} toward $z \sim 6-8$ (Kageura et al. 2025; Umeda et al. 2025; Umeda et al. 2025). We use these studies only to motivate the compressed parameter ranges explored below, not as a claim that the true reionization history is uniquely determined.

Figure 1 illustrates this motivation by comparing a more traditional reionization history with a late-reionization history inspired by recent observational analyses. The purpose of this comparison is only to indicate the type of target histories emphasized in the present work.

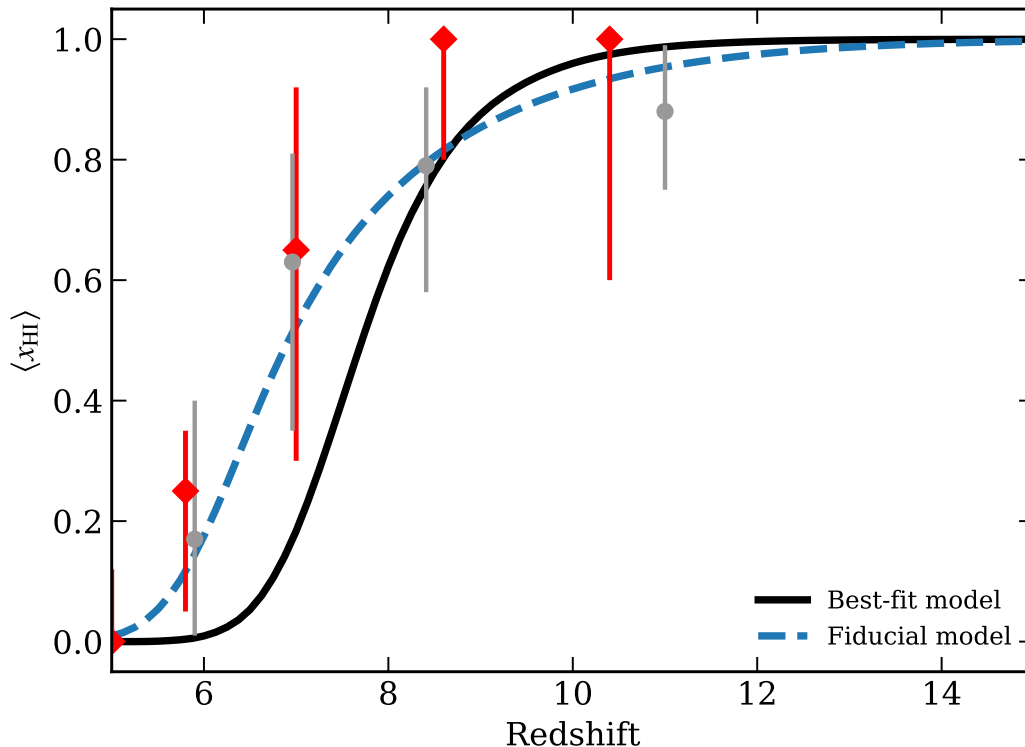


Fig. 1: Comparison between a more traditional reionization history and a late-reionization history motivated by recent JWST-based analyses (Umeda et al. 2025; Kageura et al. 2025). The black solid curve shows a best-fit late-reionization model, while the blue dashed curve shows a fiducial faint-galaxy-dominated history. Symbols denote observationally inferred neutral fractions from the cited studies.

2.3 21 cm power spectrum as the observable

For interferometric observations, the 21 cm power spectrum is the natural summary statistic, because radio arrays measure Fourier modes of the sky brightness rather than the sky-averaged signal directly (Furlanetto & Briggs 2004; Zaldarriaga et al. 2004; Morales & Wyithe 2010; Koopmans et al. 2015). Following

Furlanetto et al. (2006) and Mesinger (2019), we define the brightness-temperature fluctuation field as

$$\delta T_{21}(\mathbf{x}) = \delta T_b(\mathbf{x}) - \langle \delta T_b \rangle, \quad (6)$$

and its power spectrum by

$$\langle \delta T_{21}(\mathbf{k}_1) \delta T_{21}^*(\mathbf{k}_2) \rangle = (2\pi)^3 \delta_D(\mathbf{k}_1 - \mathbf{k}_2) P_{21}(k_1). \quad (7)$$

The dimensionless power spectrum is then

$$\Delta_{21}^2(k) = \frac{k^3}{2\pi^2} P_{21}(k), \quad (8)$$

which has units of mK^2 .

The 21 cm power spectrum is sensitive to the evolving topology of ionized regions, the global neutral fraction, and the thermal state of the IGM. Its scale dependence is therefore physically informative: on relatively large scales, the signal is more directly related to the growth and overlap of ionized bubbles, whereas on smaller scales it becomes increasingly sensitive to local morphology and substructure (Zaldarriaga et al. 2004; Furlanetto et al. 2006; Morales & Wyithe 2010; Koopmans et al. 2015).

In this work, we focus on the redshift evolution of the dimensionless 21 cm power spectrum at fixed wavenumber, denoted by $\Delta_{21}^2(k, z)$. The scale dependence of this statistic reflects the characteristic sizes of ionized regions and the evolving contrast between neutral and ionized gas. On relatively large scales, the power spectrum is more directly linked to the global progress of reionization, whereas on smaller scales it becomes increasingly sensitive to local morphology and substructure (Zaldarriaga et al. 2004; Furlanetto et al. 2006; Morales & Wyithe 2010; Koopmans et al. 2015). This scale dependence is important for interpreting how different Fourier modes trace the evolving ionization structure of the intergalactic medium. Figure 2 shows the redshift evolution of $\Delta_{21}^2(k, z)$ for the fixed- k trajectories considered in this work.

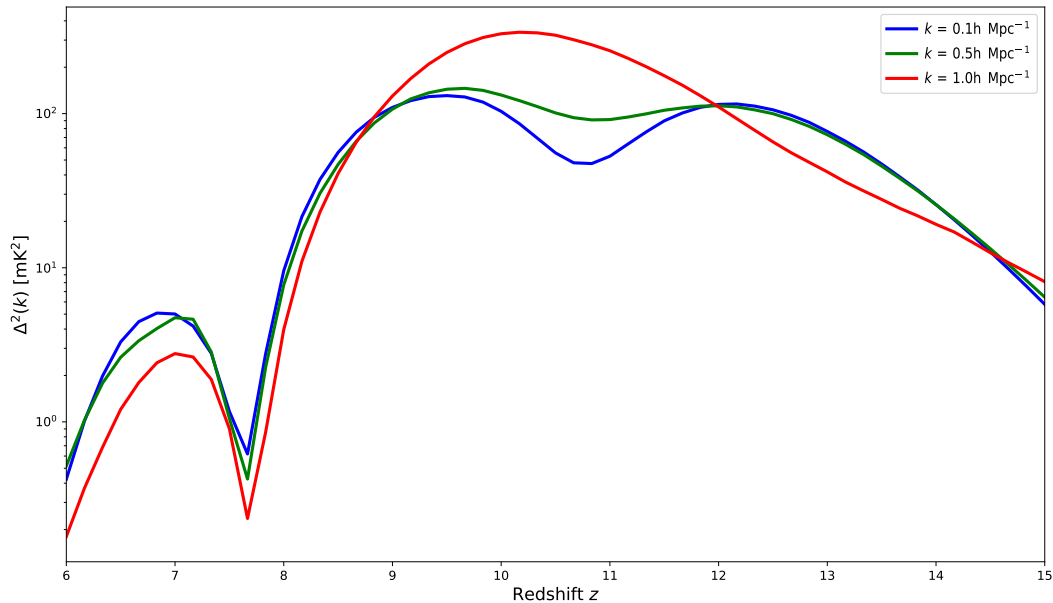


Fig. 2: Redshift evolution of the dimensionless power spectrum $\Delta_{21}^2(k, z)$ for the fixed- k trajectories considered in this work.

With the target quantity $x_{\text{HI}}(z)$ defined above and the observable $\Delta_{21}^2(k, z)$ introduced here, the present work studies the inverse mapping

$$\Delta_{21}^2(k, z) \longrightarrow x_{\text{HI}}(z). \quad (9)$$

We do not attempt a model-independent reconstruction; instead, this inverse relation is examined within a restricted but physically motivated three-parameter 21cmFAST model family.

3 ARTIFICIAL NEURAL NETWORK

The inverse problem considered in this work is to reconstruct the reionization history $x_{\text{HI}}(z)$ from the redshift evolution of the dimensionless 21 cm power spectrum at fixed wavenumber. The central question is, therefore, how accurately the reionization history can be reconstructed from a fixed- k 21 cm power-spectrum trajectory for the restricted set of histories generated by the three-parameter 21cmFAST setup adopted here.

We use a feed forward ANN as a mapping that maps the redshift evolution of $\Delta_{21}^2(k, z)$ at fixed k to the target reionization history. The point of this section is therefore not to review generic deep learning concepts, but to describe the specific mapping used to test whether the inverse map is sufficiently regular within this restricted three-parameter 21cmFAST setup. By the universal approximation theorem, even a network with a single hidden layer can represent a wide class of smooth nonlinear maps (Hornik et al. 1989), which is adequate for the restricted problem considered here.

3.1 Data Preparation

We generate the dataset with 21cmFAST v3.4 (Mesinger et al. 2011; Park et al. 2019; Murray et al. 2020), which uses the excursion set formalism (Furlanetto et al. 2004) to evolve the density and ionization fields and compute the corresponding 21cm signal. We vary only three astrophysical parameters and sample them with Latin hypercube sampling (LHS), following the parameterization widely used in 21cmFAST-based inference studies (Greig & Mesinger 2015):

(1) `HII_EFF_FACTOR(ζ)`: the ionizing efficiency of high z galaxies. Higher values tend to speed up reionization.

(2) `ION_Tvir_MIN(T_{vir})`: minimum virial temperature of star forming haloes, given in \log_{10} units.

(3) `R_BUBBLE_MAX(R_{mfp})`: Mean free path in Mpc of ionizing photons within ionized regions.

Motivated by the late reionization scenarios discussed in Section 2.3, we restrict the parameter ranges to those listed in Table 1. This compression is deliberate: it lets us ask how much information fixed k power-spectrum evolution carries inside a narrow but astrophysically motivated family of histories. In particular, we vary only the three parameters that most directly regulate the ionization-side reionization history in this setup—`HII_EFF_FACTOR`, `ION_Tvir_MIN`, and `R_BUBBLE_MAX`—while keeping the X-ray heating sector fixed at the default 21cmFAST values. The aim is to isolate a prior-dependent inverse problem for $x_{\text{HI}}(z)$: if X-ray heating parameters were also varied, $\Delta_{21}^2(k, z)$ would respond to both thermal and ionization histories, broadening the allowed trajectory family and introducing additional heating-ionization degeneracies that are beyond the scope of this proof-of-concept. Consequently, the analysis does not test

whether the network can disentangle a broad heating-ionization degeneracy; instead it probes a restricted inverse problem conditioned on an ionization-side prior.

Table 1: Parameter Settings for the Semi Numerical Reionization History Simulation

Symbol	Parameter Description	21cmFAST Parameter	Value Range
ζ	Ionizing Efficiency	HII_EFF_FACTOR	[260, 400]
$\log T_{\text{vir}}^{\text{min}}$	Min. Virial Temperature (log K)	ION_Tvir_MIN	[5.45, 5.85]
R_{mfp}	Max. Mean Free Path (Mpc)	R_BUBBLE_MAX	[10, 65]

In the implementation scripts, each simulated realization contributes one fixed k trajectory sampled at 97 redshift bins spanning $z = 6\text{--}30$. We generate 200 realizations for each of the three fixed wavenumbers considered here ($k = 0.1, 0.5, \text{ and } 1.0 h \text{ Mpc}^{-1}$), for a total of 600 trajectories. Accordingly, the ANN input and output vectors both have dimension 97. For the noisy recovery pipeline supplied with the paper, the explicit simulation and noise generation script is written for the representative case $k_{\text{target}} = 0.1 h \text{ Mpc}^{-1}$, while the same 97-dimensional architecture is used for the scale-dependent tests shown in the manuscript.

The simulation script uses `HII_DIM=200` and `BOX_LEN=300`. The raw power spectrum is computed from the 21cm brightness temperature cube with 100 logarithmic k bins between 0.05 and $1.5 h \text{ Mpc}^{-1}$, and the nearest bin to the target k is converted to the dimensionless form $\Delta_{21}^2(k)$. All ANN inputs discussed below are these fixed- k $\Delta_{21}^2(k, z)$ trajectories.

3.2 Artificial Neural Network Architecture

Our ANN is a standard multilayer perceptron with one hidden layer. In the implementation used here, the network maps a 97-dimensional fixed- k $\Delta_{21}^2(k, z)$ trajectory to a 97-dimensional reconstructed reionization history. The architecture consists of an input layer with 97 nodes, one hidden layer with 128 neurons, a ReLU activation function, and an output layer with 97 nodes. In code, this corresponds to the sequence `Linear(97, 128) → ReLU → Linear(128, 97)`.

Let x_j denote the input power-spectrum trajectory sampled on the redshift grid. The pre-activation of the hidden layer is

$$s_i = \sum_{j=1}^{N_{\text{in}}} \omega_{ij}^{(1)} x_j + b_i^{(1)}, \quad (10)$$

where $N_{\text{in}} = 97$, $\omega_{ij}^{(1)}$ are the first-layer weights, and $b_i^{(1)}$ are the corresponding biases. The activated hidden representation is

$$t_i = \text{ReLU}(s_i). \quad (11)$$

The output layer then gives

$$y_i = \sum_{j=1}^{N_{\text{h}}} \omega_{ij}^{(2)} t_j + b_i^{(2)}, \quad (12)$$

where $N_{\text{h}} = 128$, and y_i denotes the reconstructed neutral fraction at the i -th redshift bin.

The role of the ANN is therefore to learn a nonlinear map from $\Delta_{21}^2(k, z)$ to $x_{\text{HI}}(z)$ within the adopted training family. We do not interpret the network as discovering a model-independent reionization history from first principles.

3.3 Back Propagation Algorithm

We optimize the network weights with standard back propagation (Rumelhart et al. 1986). The total training cost is

$$E = \sum_{n=1}^{N_{\text{train}}} E_n = \sum_{n=1}^{N_{\text{train}}} \left[\frac{1}{2} \sum_{i=1}^m (y_{i,n} - d_{i,n})^2 \right] \quad (13)$$

where N_{train} is the number of training samples, m is the number of output neurons, y is the ANN prediction, and d is the target. The weight update follows

$$\Delta\omega_{i,j}^{(l)} = -\eta \frac{\partial E}{\partial \omega_{i,j}^{(l)}} = -\eta \sum_{n=1}^{N_{\text{train}}} \frac{\partial E}{\partial \omega_{i,j}^{(l)}} \quad (14)$$

where η is the learning rate. For the purposes of this paper, the technical role of training is straightforward: it adjusts the inverse-mapping so that the predicted $x_{\text{HI}}(z)$ tracks the simulation target on unseen samples from the same prior family.

3.4 Experimental Settings

We use the rectified linear unit (ReLU) as the hidden layer activation function (Nair & Hinton 2010),

$$f(x) = \max(0, x) \quad (15)$$

and the mean squared error (MSE) as the training loss,

$$\text{MSE} = \frac{1}{N_{\text{train}}} \sum_{i=1}^{N_{\text{train}}} E_n \quad (16)$$

The training process is through PyTorch and run on either GPU or CPU depending on availability. The clean signal recovery uses the Adam optimizer with learning rate 10^{-2} , a maximum of 2000 epochs, and early stopping with patience 100 based on the validation loss. The thermal noise recovery keeps the same ANN architecture but switches to AdamW with learning rate 10^{-3} and weight decay 10^{-4} , using up to 10,000 epochs. In that script the SKA-like noise case uses patience 100, while the exaggerated $1000\times$ noise case uses patience 500 to tolerate larger validation loss fluctuations. In both scripts, the best checkpoint is chosen solely from the validation loss and then applied to the test set.

Figure 3 shows representative learning curves. In this study, training, validation, and diagnostic test losses are all recorded, but only the validation loss is used for checkpoint selection. We evaluate three aspects of the inverse problem on one independent test split. First, we compare reconstructions at fixed $k = 0.1, 0.5,$ and $1.0 h \text{ Mpc}^{-1}$ to test how the information content changes with scale. Second, we add an idealized foreground-free SKA1-Low-like thermal-plus-sample-variance noise model, as well as an exaggerated $1000\times$ noise stress test, to assess how stable the inverse map remains in noisier conditions. Third, because the restricted model family produces smooth S-shaped histories, we examine the transition interval $0.2 \leq x_{\text{HI}} \leq 0.8$ as a scientifically motivated test of whether the network is capturing the physically informative part of reionization rather than only the generic endpoints.

4 RESULTS

In this section we present the reconstructed reionization history $x_{\text{HI}}(z)$ inferred from fixed- k trajectories of $\Delta_{21}^2(k, z)$. Unless stated otherwise, the input trajectories are taken directly from the simulated signal, so the discussion first isolates the structure of the inverse map before observational perturbations are added.

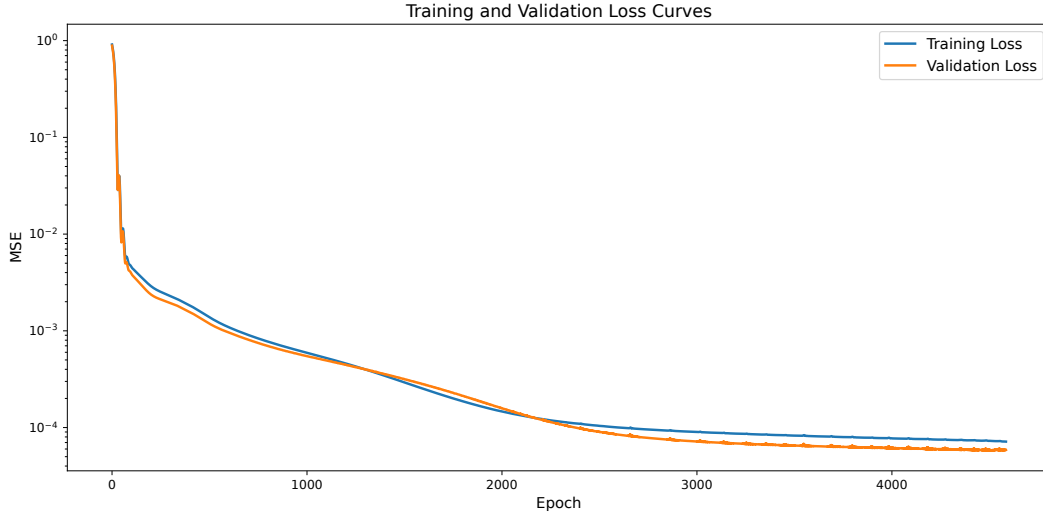


Fig. 3: Representative MSE learning curves during model optimization. Early stopping is applied using the validation set MSE, and the best validation checkpoint is retained for final evaluation.

4.1 Recovered reionization history

We reconstruct $x_{\text{HI}}(z)$ over $z = 6\text{--}15$ using the dimensionless power spectrum evaluated at fixed wavenumber. To assess the scale dependence of the inverse mapping, we compare reconstructions obtained at $k = 0.1, 0.5,$ and $1.0 h \text{ Mpc}^{-1}$. Figure 4 presents representative reconstructed histories for these three cases. One generally expects the recovery to become less accurate toward larger k , because smaller-scale power is increasingly sensitive to local ionization morphology and is therefore less directly coupled to the global progress of reionization.

Within the present dataset, however, the reconstructions remain strong even at $k = 1.0 h \text{ Mpc}^{-1}$. We do not interpret this as evidence that small-scale modes are generically sufficient. Rather, it reflects the restricted training family adopted here: once the astrophysical parameter space is compressed to three parameters, the allowed histories occupy a relatively narrow manifold of smooth curves, and even higher- k power-spectrum trajectories retain useful timing information. The apparently weak scale dependence should therefore be understood as a prior-dependent feature of the present setup.

4.2 Correlation-based metric

To summarize the similarity between the reconstructed and true histories on the independent test set, we use the correlation coefficient (CC),

$$CC = \frac{\sum_{i=1}^{N_z} (y_{\text{true},i} - \bar{y}_{\text{true}})(y_{\text{ANN},i} - \bar{y}_{\text{ANN}})}{\sqrt{\sum_{i=1}^{N_z} (y_{\text{true},i} - \bar{y}_{\text{true}})^2} \sqrt{\sum_{i=1}^{N_z} (y_{\text{ANN},i} - \bar{y}_{\text{ANN}})^2}}, \quad (17)$$

where $y_{\text{true},i}$ and $y_{\text{ANN},i}$ denote the true and reconstructed neutral fractions at redshift z_i , and N_z is the number of redshift bins. The overbars denote redshift averages. Although the Pearson correlation coefficient is often introduced in the context of linear relations and linear fitting, its normalized form can also be used as a profile-reproduction diagnostic for two discretized histories. We use it in this latter sense: after the true and reconstructed histories are sampled on the same redshift grid, CC measures how well their mean-subtracted variations are aligned across redshift. A high CC therefore indicates that the ANN reproduces

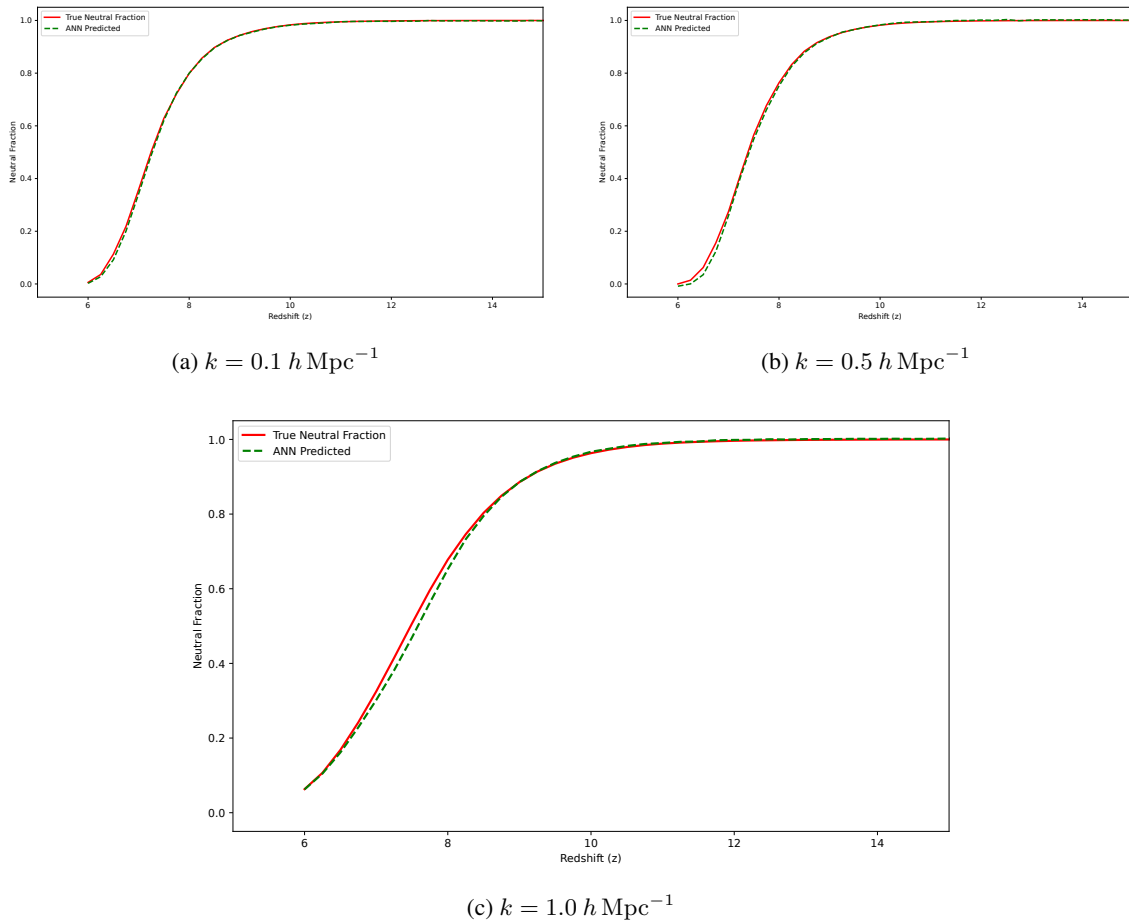


Fig. 4: Reconstructed reionization histories using fixed- k trajectories of $\Delta_{21}^2(k, z)$ at three representative scales.

the overall redshift-dependent shape of the target history, but it should not be interpreted as implying that $x_{\text{HI}}(z)$ itself is linear in redshift.

This use is justified only as a complementary measure of reconstruction fidelity, because CC is insensitive to some errors that are physically important for reionization. In particular, smooth monotonic histories can yield high CC values even when the midpoint or duration of the transition is imperfectly recovered, and an affine rescaling of a curve can leave CC nearly unchanged. We therefore use CC to summarize global shape agreement, while MAE, RMSE, z_{50} , and Δz are evaluated separately below to quantify absolute reconstruction accuracy and transition-specific errors.

Using CC in this complementary sense, we next summarize how the global shape agreement changes with scale. Figure 5 shows the CC distributions for the reconstructed reionization histories obtained from the redshift evolution of the fixed- k power spectrum at $k = 0.1, 0.5,$ and $1.0 h \text{ Mpc}^{-1}$. For the two lower- k cases, corresponding to larger spatial scales, the distributions are narrowly concentrated at high CC values, consistent with the visual impression in Figure 2 and with the expectation that these modes are more directly linked to the growth and topology of ionized regions.

At $k = 1.0 h \text{ Mpc}^{-1}$, the CC values also remain high, but this should not be interpreted as evidence for reconstruction quality comparable to the lower- k cases. As already seen in Figure 2, the recovered histories at this scale show visibly larger scatter and less faithful tracking of the transition region. This

apparent tension reflects the limitation discussed above: CC mainly measures agreement in the overall monotonic profile and is relatively insensitive to moderate mismatches in the exact midpoint and width of the transition. Within the restricted three-parameter prior adopted here, most histories are smooth and share a similar global form, so even noticeably degraded reconstructions can still yield high CC values. We therefore interpret the $k = 1.0 h \text{ Mpc}^{-1}$ result as showing that the network can still recover the broad reionization trend within our restricted three-parameter simulation set, rather than as evidence that high- k power spectra alone generally provide a precise reconstruction of the reionization history.

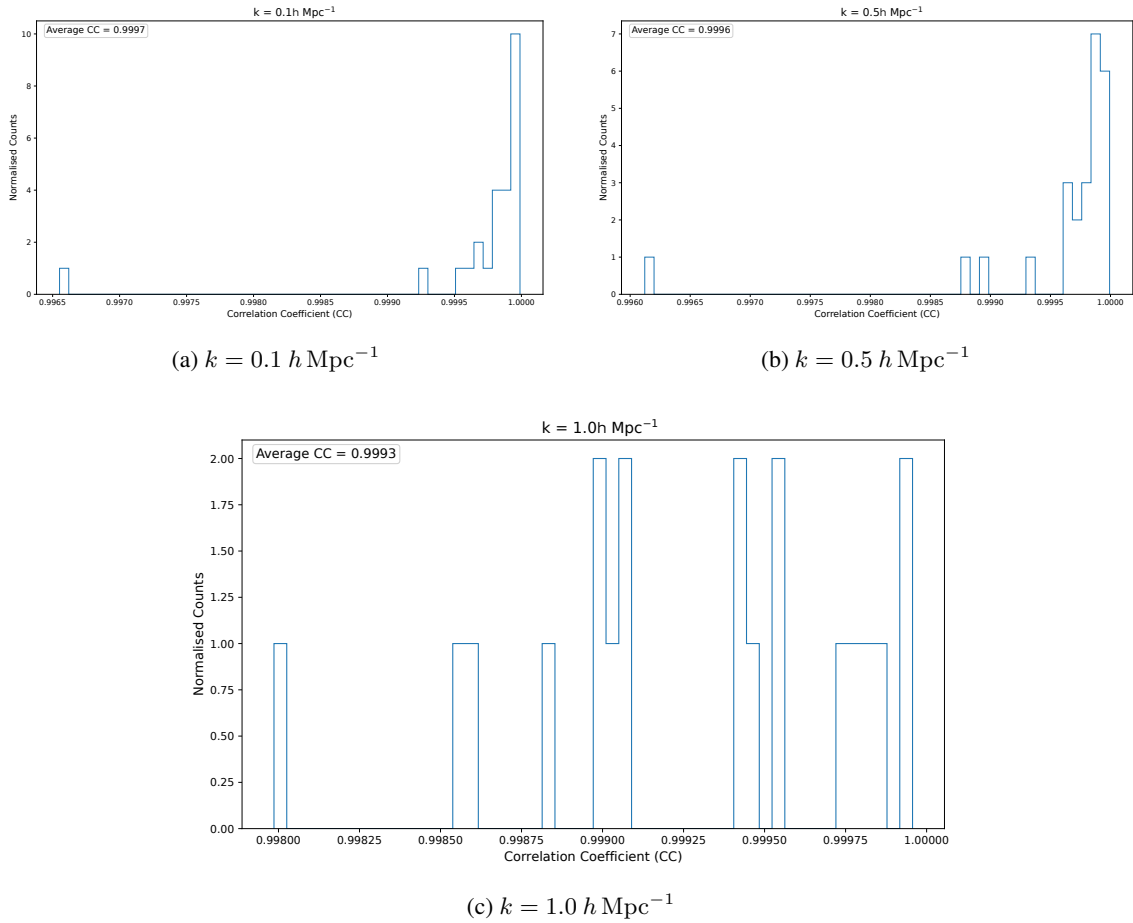


Fig. 5: Distribution of correlation coefficients for reconstructions from fixed- k $\Delta_{21}^2(k, z)$ trajectories at three representative scales.

4.3 Recovery with idealized observational noise

So far we have considered the noise-free case, in which the input power-spectrum trajectories contain no observational noise. However, real observations are affected by thermal noise, foreground contamination, calibration systematics, and other instrumental effects. In this section, we consider a more realistic but still idealized case by adding noise to the 21 cm power spectrum before using it as the ANN input. Specifically, we include only a foreground-free combination of thermal noise and sample variance in order to test how stable the inverse mapping remains under a limited observational perturbation model.

The sensitivity of a radio interferometer to the 21cm power spectrum is determined by the array configuration, integration time, and system temperature. Following the standard formalism derived in previous studies (McQuinn et al. 2006; Mao et al. 2008; Parsons et al. 2012; Mao et al. 2013), we express the thermal noise power spectrum for a single Fourier mode \mathbf{k} as:

$$P_{\text{th,1mode}}(k, \mu) \approx \frac{X^2 Y \Omega_{\text{fov}} T_{\text{sys}}^2}{t_{\text{int}} n(k_{\perp}) A_e}, \quad (18)$$

where $X^2 Y$ converts the interferometric bandwidth and solid angle into comoving volume units (see Furlanetto et al. 2006), with $X \approx d_A^2$ (comoving angular diameter distance squared) and $Y \approx \lambda_{21}^2 (1+z)^2 / H(z)$. $\Omega_{\text{fov}} \approx \lambda^2 / A_e$ is the solid angle of the primary beam field of view, A_e is the effective collecting area per station, and t_{int} represents the total integration time. $n(k_{\perp})$ denotes the number density of baselines in the uv plane that are sensitive to the transverse wavenumber $k_{\perp} = k \sqrt{1 - \mu^2}$, where $\mu = \cos \theta$ is the cosine of the angle between the wavevector \mathbf{k} and the line of sight. A high baseline density in the array core significantly enhances sensitivity to large scale structures (e.g., Parsons et al. 2012; Koopmans et al. 2015).

The system temperature, T_{sys} , is the sum of the receiver temperature and the sky brightness temperature:

$$T_{\text{sys}}(\nu) = T_{\text{rcvr}} + T_{\text{sky}}(\nu). \quad (19)$$

At the low frequencies relevant to the Epoch of Reionization (EoR) and Cosmic Dawn, the system noise is dominated by the Galactic synchrotron background. We model the sky temperature as a power law following Haslam et al. (1982) and DeBoer et al. (2017):

$$T_{\text{sky}}(\nu) \approx 60 \left(\frac{\nu}{300 \text{ MHz}} \right)^{-2.55} \text{ K}. \quad (20)$$

We assume a receiver temperature of $T_{\text{rcvr}} \approx 100 \text{ K}$, consistent with SKA1-Low design specifications (Dewdney et al. 2009; Braun et al. 2019).

Since the 21cm signal is isotropic (after accounting for redshift space distortions), we estimate the spherically averaged power spectrum sensitivity in a spherical shell of width Δk . The variance of the thermal noise for a bin centered at k is given by the inverse variance weighting of all modes in the shell (Lidz et al. 2011; Mao et al. 2013):

$$P_{\text{thermal}}(k) = \left[\sum_{\mu} \frac{N_c(k, \mu)}{P_{\text{th,1mode}}^2(k, \mu)} \right]^{-1/2}, \quad (21)$$

where $N_c(k, \mu)$ is the number of independent modes in the k shell region defined by k , μ , and logarithmic bin width $\epsilon = \Delta k / k$. Specifically, $N_c \approx \epsilon k^3 \Delta \mu \cdot V_{\text{survey}} / (4\pi^2)$, where V_{survey} is the survey volume.

In addition to thermal noise, the precision of power spectrum measurements is fundamentally limited by cosmic variance (sample variance), which arises from the finite volume surveyed. This is particularly dominant at large scales (small k). The error contribution from cosmic variance is estimated as:

$$P_{\text{cv}}(k) = \frac{P_{21}(k)}{\sqrt{N_{\text{modes}}}}, \quad (22)$$

where N_{modes} is the total number of independent Fourier modes in the upper half of the k shell.

The total observational uncertainty is the quadrature sum of the thermal noise and cosmic variance:

$$\sigma_P(k) = \sqrt{P_{\text{thermal}}^2(k) + P_{\text{cv}}^2(k)}. \quad (23)$$

Although the sensitivity expressions above are conventionally written for P_{21} , the actual ANN inputs are the corresponding dimensionless trajectories $\Delta_{21}^2(k, z)$. We therefore construct the noisy inputs in that same normalization by adding a Gaussian realization to the dimensionless signal trajectory:

$$\Delta_{\text{obs}}^2(k, z) = \Delta_{21}^2(k, z) + N_{\Delta z}(k, z). \quad (24)$$

For the noise realization, we adopt parameters representative of an idealized foreground-free SKA1-Low-like sensitivity calculation targeting the EoR (Dewdney et al. 2009; Braun et al. 2019; Shimabukuro 2025). The adopted observational specifications and analysis assumptions are summarized in Table 2.

Table 2: SKA1-Low-like observational specifications adopted for the noise model.

Item	Specification
Array layout	Compact 224-station hexagonal core within radius 500 m (core diameter ~ 1000 m), with minimum baseline 60 m and maximum retained baseline 1000 m.
Primary beam	Gaussian beam with reference frequency 150 MHz and dish size 35 m.
Site and receiver	Observatory latitude -26.8° and receiver temperature $T_{\text{rcvr}} = 100$ K.
Integration time	Total $t_{\text{int}} = 1000$ hours, implemented as 100 observing days with 10 hours per day.
Field of view	Single-beam FWHM $\sim 3.5^\circ$ at $z \sim 8$.
Bandwidth	$B = 10$ MHz per redshift bin.
Effective area	$A_e \approx 421 \text{ m}^2$ at $z \sim 8$, scaling with frequency as λ^2 .
k -binning	Logarithmic step size $\epsilon = \delta k/k = 0.1$.
Noise assumption	Foreground-free sensitivity calculation, with random Gaussian realizations drawn from the 1D thermal-plus-sample-variance uncertainty at the target k .

For each redshift, we first calculate the sensitivity at $\nu = 1420/(1+z)$ MHz, extract the nearest 1D sensitivity bin to the target k , and draw one Gaussian realization for the SKA-like case. Our noise estimates are consistent with previous studies (e.g., Koopmans et al. 2015). For the idealized SKA1-Low-like setup adopted here, the signal remains larger than the thermal-noise contribution across much of the redshift range for the scales considered. Within this favorable signal-to-noise regime, and still within the compressed three-parameter model family, the inverse mapping from $\Delta_{21}^2(k, z)$ to $x_{\text{HI}}(z)$ remains reasonably stable.

We also examine reconstructed histories over the displayed range $z = 6\text{--}15$ when noise is added according to the idealized SKA1-Low-like specification, together with an amplified case in which the thermal-noise amplitude is multiplied by 10^3 as a stress test of a much less favorable regime. In other words, the “1000 \times SKA” case denotes the same SKA-like noise model but with the noise standard deviation scaled up by a factor of 10^3 . This amplified case is not intended as a quantitative model of any specific instrument.

Figure 6 shows a representative reconstruction of $x_{\text{HI}}(z)$ from noisy fixed- k power-spectrum input. For the idealized SKA-like noise level, the reconstructed history remains close to the true curve throughout the transition, indicating that the network recovers the overall monotonic form and an approximately correct midpoint in this favorable regime. By contrast, the 1000 \times noise stress test shows visibly larger deviations, especially near the low-neutral-fraction end and around the midpoint of the transition, although it still

preserves the coarse S-shaped trend. This visual comparison motivates the more systematic error analysis below.

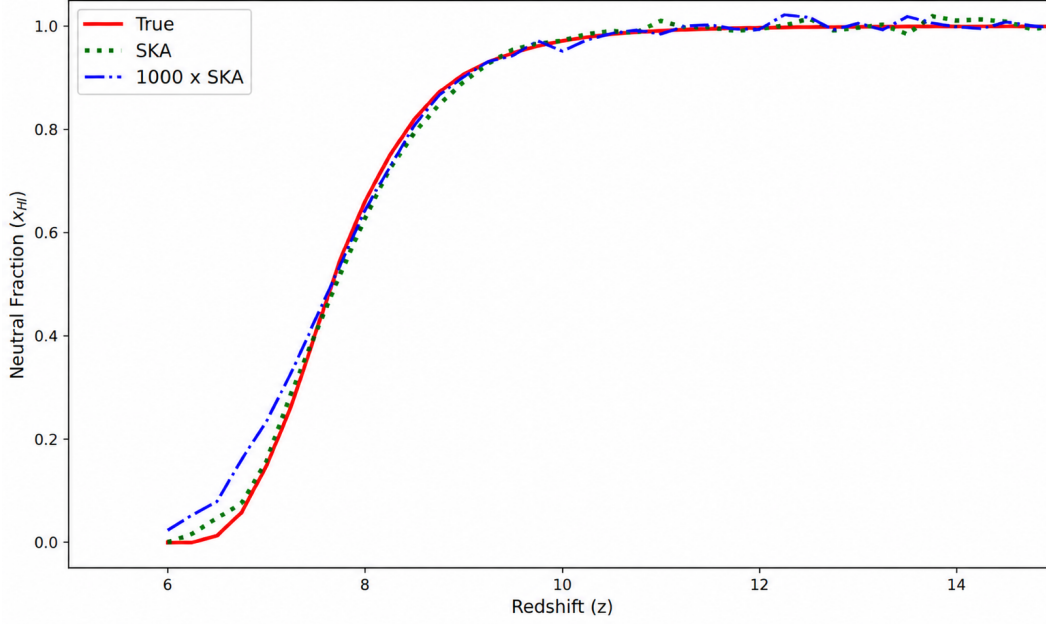


Fig. 6: Representative reconstruction of the neutral-fraction history from noisy fixed- k power-spectrum input over $z = 6$ – 15 . The red solid curve shows the true history, the green dotted curve shows the reconstruction obtained with the idealized SKA1-Low-like noise realization, and the blue dash-dotted curve shows the reconstruction for the exaggerated “1000× SKA” stress test, i.e., the same SKA-like noise model with the noise amplitude increased by a factor of 10^3 .

Because the restricted parameter space produces smooth S-shaped histories, whole curve metrics alone may overstate what the network has learned. The physically most informative regime is the transition interval, where the ionized fraction changes rapidly. We therefore re-evaluate the reconstruction specifically in the range $0.2 \leq x_{\text{HI}} \leq 0.8$.

We evaluate three physically meaningful aspects of the reconstruction within this interval: the neutral-fraction history $x_{\text{HI}}(z)$ itself, the reionization midpoint z_{50} , and the duration Δz . For the history, we quantify the reconstruction error using the mean absolute error (MAE) and the root-mean-square error (RMSE) computed from the x_{HI} residuals within the transition interval. We also track the signed residual mean (bias), median, and standard deviation. For the derived summary quantities, we evaluate the midpoint and duration errors in redshift units.

MAE measures the mean absolute difference between the predicted and true neutral fractions:

$$\text{MAE} = \frac{1}{N_{\text{test}} N_z} \sum_{n=1}^{N_{\text{test}}} \sum_{i=1}^{N_z} \left| y_{\text{true},i}^{(n)} - y_{\text{ANN},i}^{(n)} \right|. \quad (25)$$

RMSE is defined as

$$\text{RMSE} = \sqrt{\frac{1}{N_{\text{test}} N_z} \sum_{n=1}^{N_{\text{test}}} \sum_{i=1}^{N_z} \left(y_{\text{true},i}^{(n)} - y_{\text{ANN},i}^{(n)} \right)^2}. \quad (26)$$

Like MSE, RMSE gives greater weight to large residuals than MAE.

For the neutral-fraction history, we define the signed residual as $y_{\text{true}} - y_{\text{ANN}}$, so positive values indicate that the ANN underestimates x_{HI} on average. For the derived summary quantities, we instead define signed errors as predicted minus true.

The midpoint error is defined as

$$\text{Error}_{z_{50}} = z_{50}^{\text{ANN}} - z_{50}^{\text{true}}. \quad (27)$$

For the duration, we use the same positive-duration convention as in Equation (5),

$$\Delta z \equiv z_{75} - z_{25}, \quad (28)$$

where $x_{\text{HI}}(z_{75}) = 0.75$ and $x_{\text{HI}}(z_{25}) = 0.25$. The duration error is then defined as

$$\text{Error}_{\Delta z} = \Delta z^{\text{ANN}} - \Delta z^{\text{true}}. \quad (29)$$

Figures 7–12 summarize the error distributions in the transition regime, and Table 3 collects the main statistics.

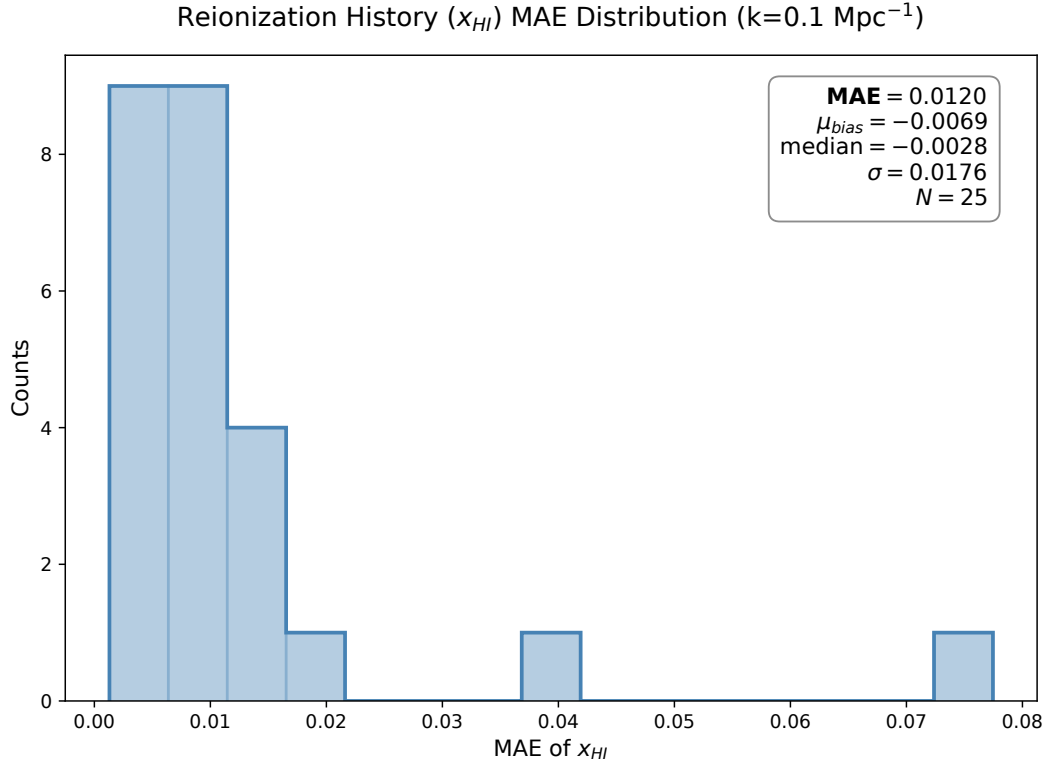


Fig. 7: MAE distribution for the reconstructed reionization history in the transition interval using noisy inputs at $k = 0.1 \text{ h Mpc}^{-1}$.

Table 3 summarizes representative one-split performance for the three key reionization descriptors, evaluated within the physically most informative transition interval $0.2 \leq x_{\text{HI}} \leq 0.8$ for the representative noisy $k = 0.1 \text{ h Mpc}^{-1}$ test subset. These numbers should be regarded as representative rather than as a fully converged estimate of the population-level reconstruction accuracy. For the reionization history itself, the network achieves a small absolute reconstruction error (MAE = 0.0120 and RMSE = 0.0139), indicating that the predicted $x_{\text{HI}}(z)$ tracks the target curves closely across the transition regime.

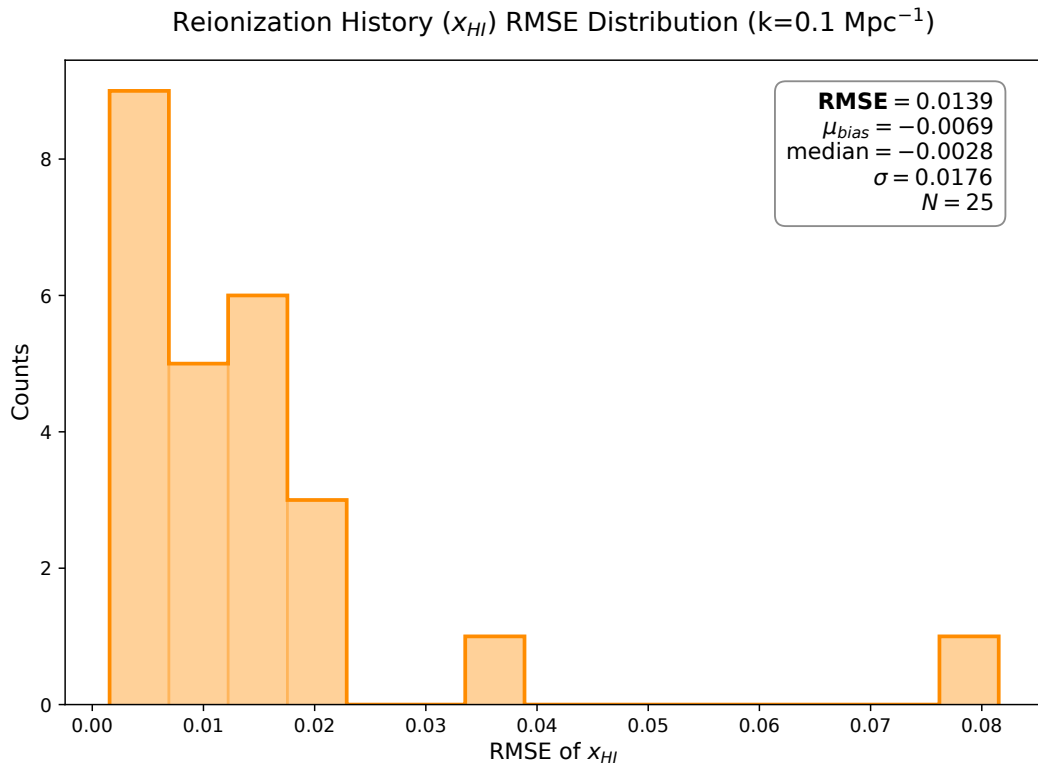


Fig. 8: RMSE distribution for the reconstructed reionization history in the transition interval using noisy inputs at $k = 0.1 h \text{ Mpc}^{-1}$.

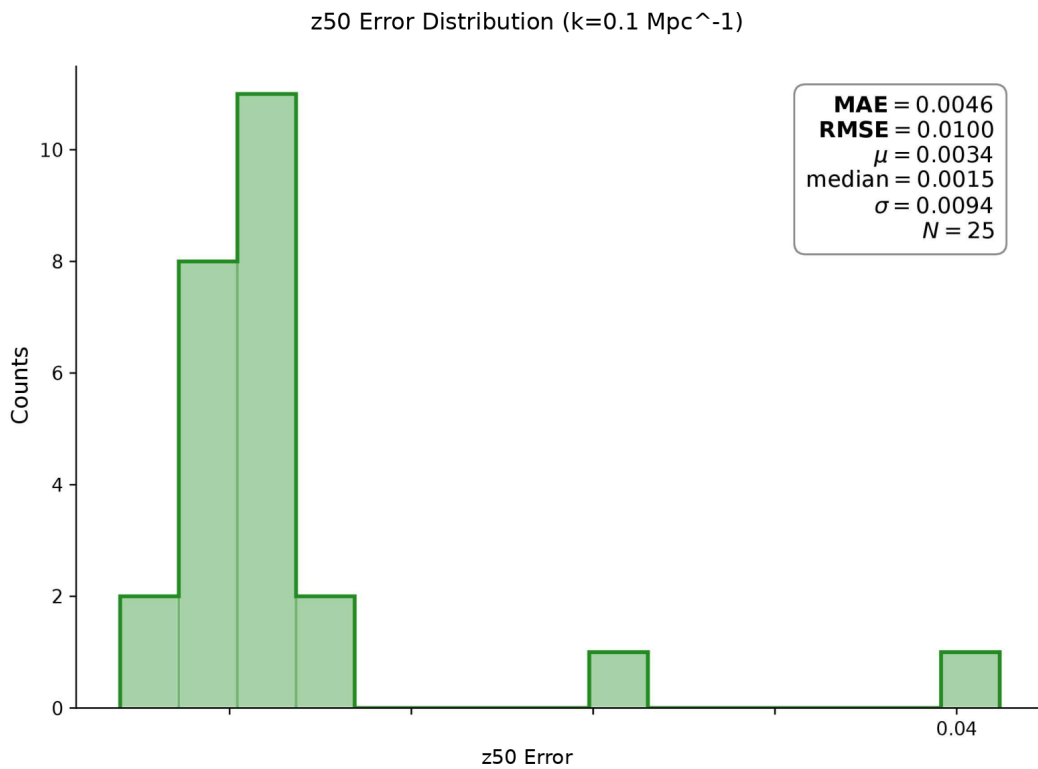


Fig. 9: Distribution of the signed midpoint error, $z_{50}^{ANN} - z_{50}^{true}$, in redshift units.

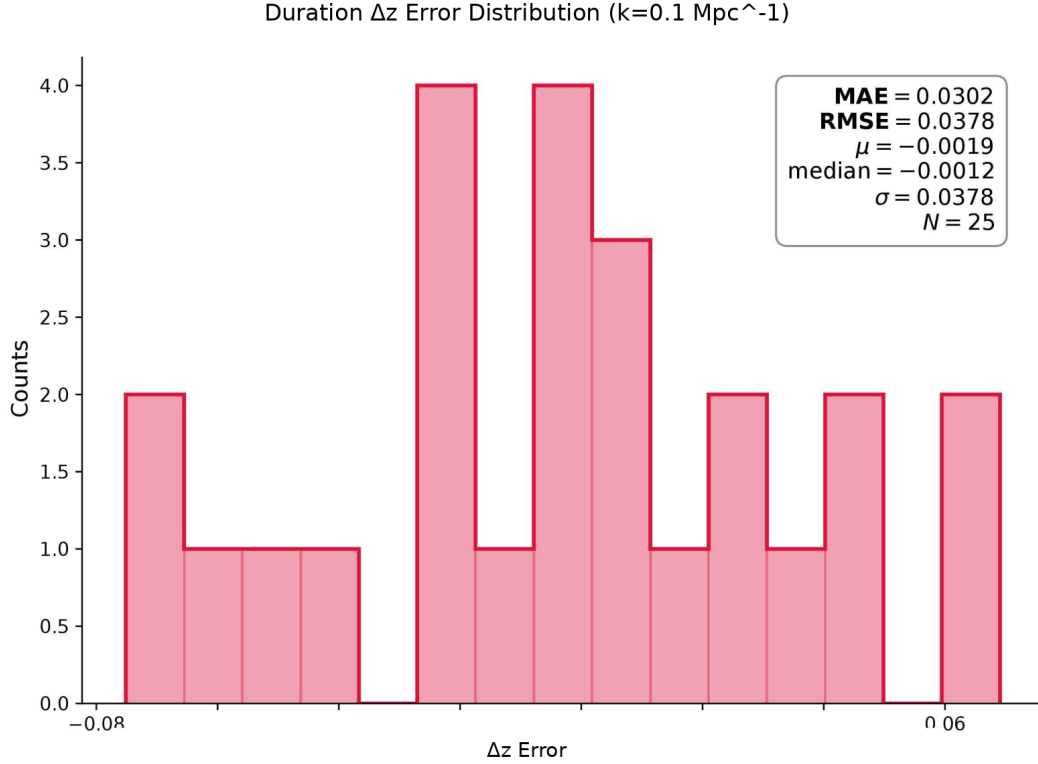


Fig. 10: Distribution of the signed duration error, $\Delta z^{\text{ANN}} - \Delta z^{\text{true}}$, in redshift units.

Table 3: Representative performance summary for one independent test subset ($N = 25$ trajectories) for the three main reionization descriptors.

Parameter	MAE	RMSE	Bias (μ)	Median	σ	N
Reionization History (x_{HI})	0.0120	0.0139	-0.0069	-0.0028	0.0176	25
Reionization Midpoint (z_{50})	0.0046	0.0100	0.0034	0.0015	0.0094	25
Reionization Duration (Δz)	0.0302	0.0378	-0.0019	-0.0012	0.0378	25

The signed residual distribution shows a mild negative bias ($\mu = -0.0069$; median = -0.0028) with a modest scatter ($\sigma = 0.0176$), implying a slight tendency to overestimate the neutral fraction on average under the adopted sign convention. When propagated to summary parameters, the midpoint redshift is recovered more accurately than the duration: the error statistics for z_{50} are MAE = 0.0046 and RMSE = 0.0100, with a small positive bias ($\mu = 0.0034$, median = 0.0015) and a tight dispersion ($\sigma = 0.0094$). In contrast, the duration Δz is more challenging, with larger errors (MAE = 0.0302, RMSE = 0.0378) and a broader spread ($\sigma = 0.0378$), although the mean bias remains close to zero ($\mu = -0.0019$; median = -0.0012). This asymmetry between midpoint and duration is the main scientific message of the representative noisy test: within the restricted prior, fixed- k power-spectrum evolution is a stronger estimator of reionization timing than of the detailed width of the transition.

Overall, these representative noisy-input results support a cautious conclusion. Within the adopted model family and the favorable signal-to-noise regime of the idealized foreground-free noise model considered here, the inverse mapping from $\Delta_{21}^2(k, z)$ to $x_{\text{HI}}(z)$ appears reasonably stable, especially for midpoint-

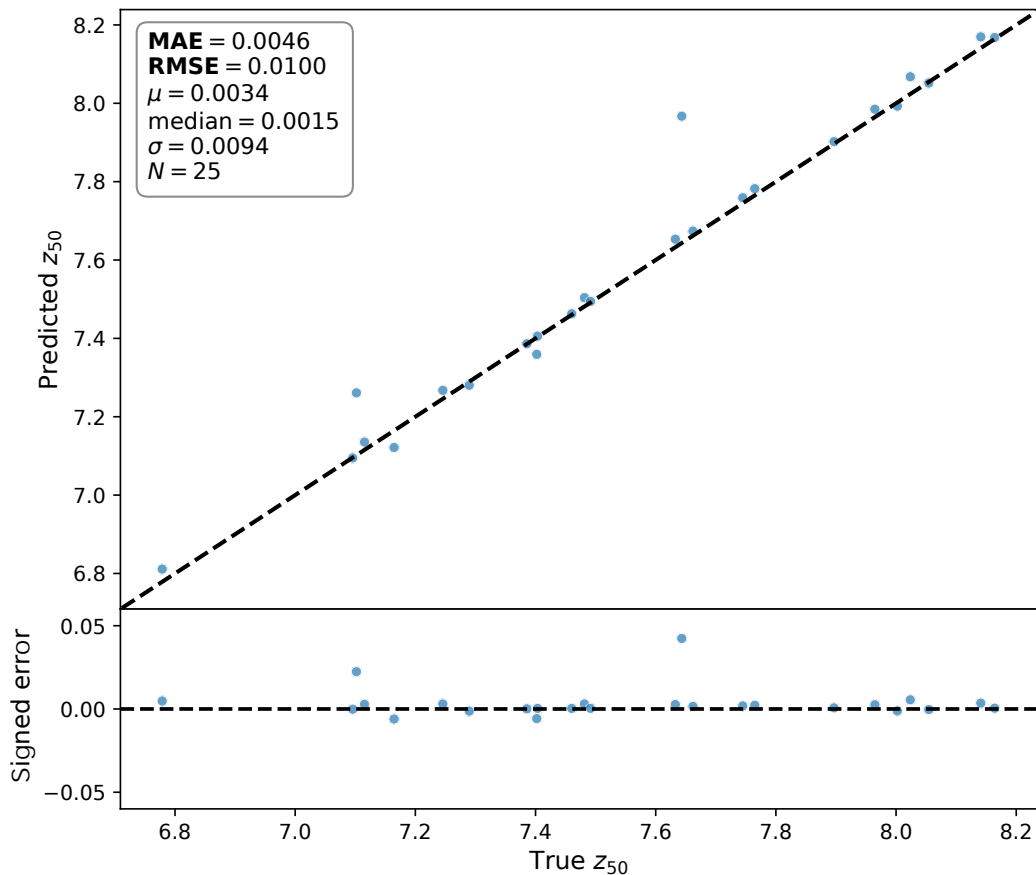


Fig. 11: Scatter plot of midpoint recovery for the reconstructed reionization history. The lower panel shows the signed difference $z_{50}^{\text{ANN}} - z_{50}^{\text{true}}$ in redshift units.

related quantities. Duration estimates are less precise and are therefore more sensitive to both noise and prior assumptions.

5 SUMMARY & DISCUSSION

We have investigated whether fixed- k trajectories of the dimensionless 21 cm power spectrum, $\Delta_{21}^2(k, z)$, can be used to reconstruct the reionization history $x_{\text{HI}}(z)$ within a restricted, physically motivated three-parameter model by 21cmFAST. The main result of this work is that, within the adopted three-parameter 21cmFAST prior, fixed- k trajectories of $\Delta_{21}^2(k, z)$ contain enough information to reconstruct the reionization history $x_{\text{HI}}(z)$ with a compact ANN. In the representative tests presented here, the network recovers the timing of reionization more reliably than the detailed width of the transition. This conclusion should be interpreted within the scope of the present setup, where the network serves as a prior-dependent neural-network-based reconstructor rather than a model-independent framework.

Within the present setup, the lower- k trajectories provide the clearest connection to the global evolution of reionization. The reconstructions at $k = 0.1$ and 0.5 h Mpc^{-1} are broadly consistent with the expectation that larger-scale modes trace the global ionization trend more directly. The reconstructions at $k = 1.0 \text{ h Mpc}^{-1}$ remain reasonably good within the present setup. We interpret this as a consequence of the restricted training family adopted here, in which the allowed histories occupy a relatively narrow manifold of smooth curves. The weak scale dependence seen in the present calculations should therefore be

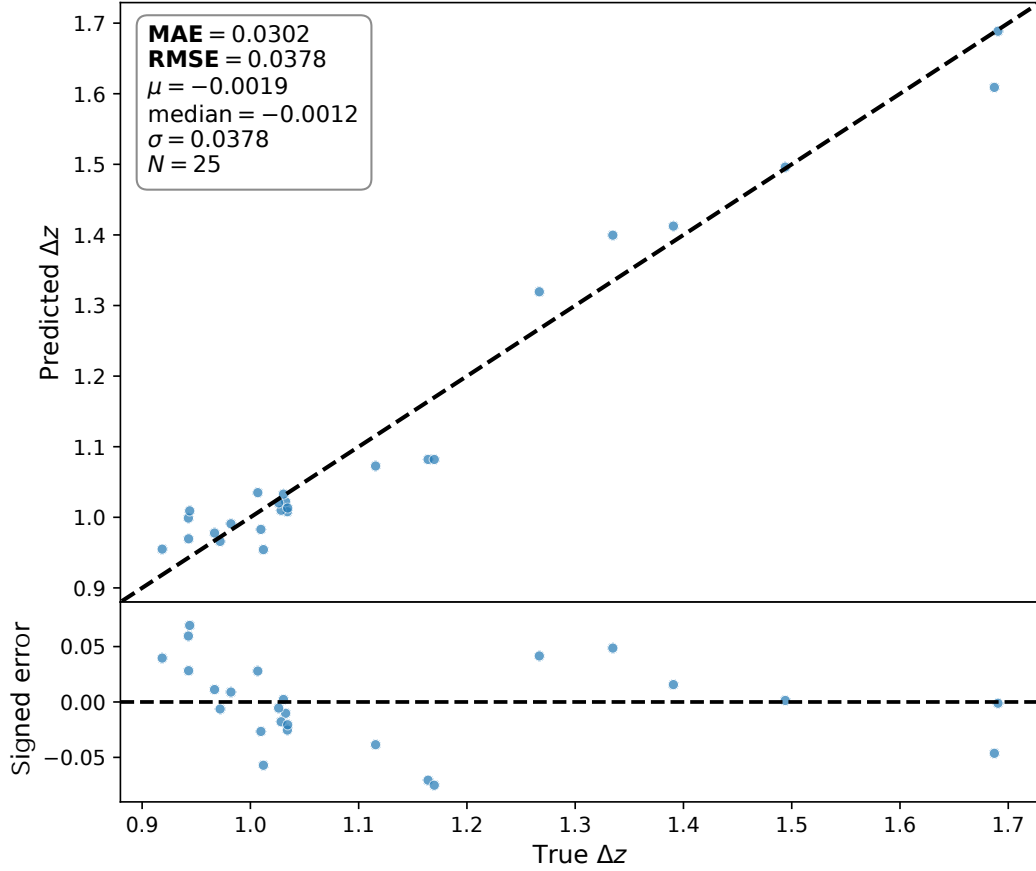


Fig. 12: Scatter plot of duration recovery for the reconstructed reionization history. The lower panel shows the signed difference $\Delta z^{\text{ANN}} - \Delta z^{\text{true}}$ in redshift units.

understood as a prior-dependent feature of the adopted model space; in a broader astrophysical parameter space, a stronger scale dependence may emerge.

The most informative result comes from the transition-interval analysis. In the representative one-split test reported here, the midpoint z_{50} is recovered substantially more accurately than the duration Δz . This indicates that fixed- k power-spectrum trajectories retain stronger information about the timing of reionization than about the detailed width of the transition, at least within the adopted prior. In that sense, the present calculation is best interpreted as an information-structure result for a restricted inverse problem.

The noise tests lead to a similarly qualified conclusion. In the favorable regime of the idealized foreground-free SKA1-Low-like thermal-plus-sample-variance model considered here, the reconstruction remains reasonably stable after noise is added, especially for midpoint-related quantities. This should not be interpreted as universal robustness. The network is trained on a restricted simulation prior, and its output should therefore be interpreted as reliable only within the corresponding model family.

Several steps are required before this approach can mature into a more broadly useful reconstruction tool. A key next step is to test which aspects of the present conclusion survive once the current prior compression is relaxed. In particular, it will be important to determine whether the stronger recoverability of z_{50} relative to Δz persists beyond the present restricted model family. The training set should therefore be widened to cover a broader range of reionization histories and source prescriptions. In addition, uncertainty quantification should be incorporated, so that the network can report not only a best-fit history but also a

calibrated level of confidence and, ideally, a warning when an input trajectory lies outside its reliable domain of validity. Observational realism must also be improved by propagating foreground residuals, calibration errors, mode loss, and inter-redshift covariance through end-to-end mock analyses. Such tests will clarify whether fixed- k trajectories remain sufficient in realistic applications, or whether information from multiple k -modes or more flexible compressed summaries will be required. Finally, reconstructed histories should be confronted with external probes, including CMB optical-depth constraints, Ly α -based measurements, and high-redshift galaxy observations, so that the network output can be tested in a genuinely multi-probe framework rather than treated as a stand-alone product.

Acknowledgements This work is supported by the National SKA Program of China (No.2020SKA0110401), NSFC (Grant No. 12103044), and Yunnan Provincial Key Laboratory of Survey Science with project No. 202449CE340002.

References

- Barkana, R., & Loeb, A. 2001, *Phys. Rep.*, 349, 125
- Braun, R., Bonaldi, A., Bourke, T., Keane, E., & Wagg, J. 2019, arXiv e-prints, arXiv:1912.12699
- Chen, X., & Miralda-Escudé, J. 2004, *Astrophysical Journal*, 602, 1
- Chen, X., & Miralda-Escudé, J. 2008, *Astrophysical Journal*, 684, 18
- Dayal, P., & Ferrara, A. 2018, *Phys. Rep.*, 780, 1
- DeBoer, D. R., Parsons, A. R., Aguirre, J. E., et al. 2017, *PASP*, 129, 045001
- Dewdney, P. E., Hall, P. J., Schilizzi, R. T., & Lazio, T. J. L. W. 2009, *Proceedings of the IEEE*, 97, 1482
- Fan, X., Carilli, C. L., & Keating, B. 2006, *ARA&A*, 44, 415
- Field, G. B. 1958, *Proceedings of the IRE*, 46, 240
- Field, G. B. 1959, *Astrophysical Journal*, 129, 536
- Furlanetto, S. R., & Briggs, F. H. 2004, *New Astronomy Reviews*, 48, 1039
- Furlanetto, S. R., Oh, S. P., & Briggs, F. H. 2006, *Phys. Rep.*, 433, 181
- Furlanetto, S. R., Zaldarriaga, M., & Hernquist, L. 2004, *ApJ*, 613, 1
- Greig, B., & Mesinger, A. 2015, *Monthly Notices of the Royal Astronomical Society*, 449, 4246
- Haslam, C. G. T., Salter, C. J., Stoffel, H., & Wilson, W. E. 1982, *A&AS*, 47, 1
- Hirata, C. M. 2006, *Monthly Notices of the Royal Astronomical Society*, 367, 259
- Hornik, K., Stinchcombe, M., & White, H. 1989, *Neural Networks*, 2, 359
- Kageura, Y., Ouchi, M., Nakane, M., et al. 2025, *ApJS*, 278, 33
- Koopmans, L., Pritchard, J., Mellema, G., et al. 2015, in *Advancing Astrophysics with the Square Kilometre Array (AASKA14)*, 1
- La Plante, P., & Ntampaka, M. 2019, *The Astrophysical Journal*, 880, 110
- Lidz, A., Furlanetto, S. R., Peng Oh, S., et al. 2011, *The Astrophysical Journal*, 741, 70
- Madau, P. 2017, *ApJ*, 851, 50
- Madau, P., Haardt, F., & Rees, M. J. 1999, *ApJ*, 514, 648
- Madau, P., Meiksin, A., & Rees, M. J. 1997, *ApJ*, 475, 429
- Mao, Y., D'Aloisio, A., Zhang, J., & Shapiro, P. R. 2013, *Phys. Rev. D*, 88, 081303

- Mao, Y., Tegmark, M., McQuinn, M., Zaldarriaga, M., & Zahn, O. 2008, *Phys. Rev. D*, 78, 023529
- McQuinn, M., Zahn, O., Zaldarriaga, M., Hernquist, L., & Furlanetto, S. R. 2006, *ApJ*, 653, 815
- Mesinger, A. 2019, *The Cosmic 21-cm Revolution; Charting the first billion years of our universe*
- Mesinger, A., Furlanetto, S., & Cen, R. 2011, *MNRAS*, 411, 955
- Morales, M. F., & Wyithe, J. S. B. 2010, *Annual Review of Astronomy and Astrophysics*, 48, 127
- Murray, S., Greig, B., Mesinger, A., et al. 2020, *The Journal of Open Source Software*, 5, 2582
- Nair, V., & Hinton, G. E. 2010, *Omnipress*
- Park, J., Mesinger, A., Greig, B., & Gillet, N. 2019, *MNRAS*, 484, 933
- Parsons, A. R., Pober, J. C., Aguirre, J. E., et al. 2012, *ApJ*, 756, 165
- Planck Collaboration, Aghanim, N., Akrami, Y., et al. 2020, *A&A*, 641, A6
- Pritchard, J. R., & Loeb, A. 2012, *Reports on Progress in Physics*, 75, 086901
- Robertson, B. E. 2022, *ARA&A*, 60, 121
- Rumelhart, D. E., Hinton, G. E., & Williams, R. J. 1986, *Nature*, 323, 533
- Scott, D., & Rees, M. J. 1990, *MNRAS*, 247, 510
- Shimabukuro, H. 2025, *Research in Astronomy and Astrophysics*, 25, 085017
- Shimabukuro, H., Hasegawa, K., Kuchinomachi, A., Yajima, H., & Yoshiura, S. 2023, *PASJ*, 75, S1
- Shimabukuro, H., Mao, Y., & Tan, J. 2022, *Research in Astronomy and Astrophysics*, 22, 035027
- Shimabukuro, H., & Semelin, B. 2017, *MNRAS*, 468, 3869
- Sikder, S., Barkana, R., Reis, I., & Fialkov, A. 2024, *MNRAS*, 527, 9977
- Umeda, H., Ouchi, M., Kageura, Y., et al. 2025, *arXiv e-prints*, arXiv:2504.04683
- Umeda, H., Ouchi, M., Kikuta, S., et al. 2025, *The Astrophysical Journal Supplement Series*, 277, 37
- Wouthuysen, S. A. 1952, *Astronomical Journal*, 57, 31
- Zaldarriaga, M., Furlanetto, S. R., & Hernquist, L. 2004, *Astrophysical Journal*, 608, 622